Additive Manufacturing 32 (2020) 101080

Contents lists available at ScienceDirect

Additive Manufacturing

journal homepage: www.elsevier.com/locate/addma

Full Length Article

Effects of inter layer time and build height on resulting properties of 316L stainless steel processed by laser powder bed fusion

Gunther Mohr[a,b,*], Simon J. Altenburg[a], Kai Hilgenberg[a,b]

[a] Federal Institute for Materials Research and Testing (BAM; Bundesanstalt für Materialforschung und -prüfung), Unter den Eichen 87, 12205 Berlin, Germany
[b] Institute of Machine Tools and Factory Management, Chair of Processes and Technologies for Highly Loaded Welds, Technische Universität Berlin, Straße des 17. Juni, 10623 Berlin, Germany

ARTICLE INFO

Keywords:
Laser powder bed fusion (L-PBF)
Laser beam melting (LBM)
Selective laser melting (SLM)
Dwell-time
Thermography

ABSTRACT

Laser powder bed fusion (L-PBF) is the most prominent additive manufacturing (AM) technology for metal part production. Among the high number of factors influencing part quality and mechanical properties, the inter layer time (ILT) between iterative melting of volume elements in subsequent layers is almost completely unappreciated in the relevant literature on L-PBF. This study investigates the effect of ILT with respect to build height and under distinct levels of volumetric energy density (VED) using the example of 316L stainless steel. In-situ thermography is used to gather information on cooling conditions during the process, which is followed by an extensive metallographic analysis. Significant effects of ILT and build height on heat accumulation, sub-grain sizes, melt pool geometries and hardness are presented. Furthermore, the rise of defect densities can be attributed to a mutual interplay of build height and ILT. Hence, ILT has been identified as a crucial factor for L-PBF of real part components especially for those with small cross sections.

1. Introduction

1.1. Additive manufacturing and comparability of specimens

Within the group of additive manufacturing (AM) technologies for metals, laser powder bed fusion (LPBF) has a leading position driven by aerospace, medical engineering and tool manufacturing industries [1–4]. This is due to the huge potential offered by the process inherent freedom of design, leading to improvements in the production of complex and lightweight structures and integration of functional designs [5–7]. Recently, clear criticism about inconsistent properties between specimens produced by LPBF of the same material and resulting comparability issues have been observed in the relevant literature [1]. Different part geometries as well as different processing parameters and scanning strategies, accompanied by incomplete documentation of number of parts per build, amplify the variety of published results about mechanical properties and microstructures. The result is a huge range of published values for the same materials. However, reliable and comparable information about mechanical properties and potential inhomogeneities are required for the design of safety-critical components [8]. Therefore, this study focuses on the influence of inter layer times as an aspect which is very rarely considered in L-PBF processes. Additionally, the build height as a factor of geometry is also part of the examination as are differences in volumetric energy density. A comparison of combinations of these three factors will be drawn for the widely used stainless steel 316 L.

1.2. Definition of inter layer times and related work

From conventional welding technology it is well known that temperature gradients have a huge impact on microstructural development as well as on shrinkage and formation of residual stresses. Increasing temperature gradients through higher welding velocities contribute to higher residual stresses [9]. Hence, longer times for part cooling during the process may result in higher temperature gradients and, therefore, in higher residual stresses in the layer-wise process of LPBF. In addition, fine grained microstructures can usually be expected for the resulting high cooling rates. Several studies describe approaches to decrease temperature gradients, residual stresses and crack susceptibility by using platform preheating or remelting [7,10,11].

In layer based AM, the time span between subsequent energy input at a single volume element from layer to layer influences the thermal gradients. This time is referred to as inter layer time and will be abbreviated by ILT in this study. Several synonyms of ILT are used interchangeably in the relevant literature, such as “idle time” [12,13], “time breaks” or “time delay” [14] and “dwell time” [15]. For LPBF

* Corresponding author.
E-mail address: gunther.mohr@bam.de (G. Mohr).

https://doi.org/10.1016/j.addma.2020.101080
Received 29 July 2019; Received in revised form 6 January 2020; Accepted 15 January 2020
Available online 16 January 2020

systems, the ILT consists of the time for powder recoating when no laser radiation is turned on, and the time in the exposition phase, which is needed until a particular volume element experiences laser exposition due to part scanning in a specified manner. This is summarised in Eq. (1). Hence, the ILT is normally governed by the velocity of the recoater, the number of parts to be exposed in the build volume, the area of exposition in a particular layer of a part and the scanning strategy as well as manufacturing parameters [16]. Therefore, the ILT of real components is not necessarily constant over all layers due to geometrical deviations in cross section areas per layer and differences in scanning strategies between different sized cross section areas. Consequently, ILT can be translated into an equivalent scanning area per layer, representing the area which can be scanned and exposed per layer for a given scanning velocity, hatch distance and scanning strategy within that time. The calculated equivalent scanning area per layer can be translated into a ratio of area exploitation per layer for a given machine set up with a defined build space. As long as the scanning parameters are constant over the part's geometry, the ILT is mainly driven by the size of the area to be exposed, which often differs from layer to layer. So far, no distinct applicable term for the utilisation of the powder bed area on a layer level can be found in the relevant literature. Currently, authors analysing the economic substance or presenting views on factory design use terms such as "load factor" [17], "packing density" [17], "filling of build chamber" [18], "part number per bed" [19], "bin packing" [20] or "nesting" [21]. From a more process and properties driven point of view, it is covered by the term "layout parameter" [22], and can be found to be contained in "structure to powder bed volume ratio" or "part to powder bed volume ratio" [23]. However, most of these terms consider the whole 3D volume and not only the 2D cross section area per layer. Hence, this deficiency is addressed here by introducing a new term: ratio of area exploitation per layer (RAE), as summarised in Eq. (2). RAE cannot replace the calculation of ILT, since scanning strategy and vector number can vary with structure size. Therefore, layers with same RAE can have different ILT. However, RAE can be considered as a useful estimation value for comparisons between different components prior to the definition of the scanning pattern.

$$ILT_{layer\ n} = \text{time for powder recoating} + \text{time for laser exposing in layer n} \tag{1}$$

$$RAE_{layer\ n} = \frac{\text{area of 2D cross sections of parts in layer } n}{\text{area of powder bed}} \tag{2}$$

ILT for powder bed based processes have so far been studied in only very few publications [24,25]. However, for Direct Energy Deposition (DED) processes, such as powder nozzle based laser metal deposition (LMD), some studies can be found on this subject. The most important ones are briefly summarised here:

Costa et al. [12] developed a multilayer thermo-kinetic model for LMD processes to investigate microstructural transformations of tool steel AISI 420 during the process. Thereby, short ILT has been identified as a factor which enhances the build-up of heat accumulation with resulting changes in microstructure in terms of formation of martensite.

Jendrzejewski and Sliwinski [14] pointed out by a model and coating experiments that ILT has an influence on crack susceptibility. They processed Stellite SF6 with LMD technology resulting in less cracks for shorter ILT. They mentioned decreasing ILT as a method to reduce temperature gradients during the process.

Denlinger et al. [15] conducted in-situ distortion measurements during LMD processes of walls with a final build height of 38.1 mm using Ti-6Al4V and IN625 at three different ILT, i.e., 0 s, 20 s, and 40 s. The specimens were also analysed for residual stresses. Their investigation showed a reduction of distortion and residual stresses for IN625 with increasing ILT, whereas the results were inverse for Ti-6Al-4 V.

Yadollahi et al. [13] produced cylindric specimens with a diameter of 8 mm and a height of 75 mm out of 316 L by means of LMD, using two different ILT, i.e., 10 s and 100 s. They showed differences in hardness. Lower hardness values were measured for short inter layer times compared to long times. This was also observed for compressive and tensile behaviour as a result of a decrease in cooling rate for shorter ILT, which also coarsened the microstructure. Comparisons of bottom sections of the specimens revealed an average grain size of approx. 45 µm for the long ILT and approx. 60 µm for the short ILT. For the latter, they mentioned a change of grain sizes over the build height, measuring grain sizes of approx. 140 µm in the middle and approx. 100 µm in the top region of the specimens. No significant differences were observed for the long ILT.

Torries et al. [26] examined the effect of ILT on mechanical behaviour of cylindric specimens of Ti-6Al4V manufactured by LMD at two different inter-layer times, i.e., approx. 1 s and approx. 33.5 s. They found differences in the microstructure of non-heat-treated specimens. A finer microstructure (size of alpha laths and grain boundary alpha + beta colonies) developed for longer ILT, which they attributed to lower bulk part temperatures. These resulted in higher cooling rates and steeper temperature gradients due to larger time intervals between layers, which allowed for cooling to a greater extent. For heat treated specimens they also found differences in yield strength, ductility and fatigue behaviour, receiving reduced ductility and fatigue life for longer ILT as well as higher yield strength. However, the mechanical results have to be considered very carefully, as the specimens produced with longer ILT exhibited more defects, especially lack of fusion pores. Microstructural analysis was done only in the centre of the specimens. Nevertheless, Torries et al. stress the importance of their findings for the production of AM parts: When inter-layer times are able to change the microstructure and mechanical properties, questions arise regarding the representability of specimens in relation to real part components.

Spranger et al. [27] investigated different ILT (17.5 s, 62.5 s and 126 s) for LMD production of cylindric specimens using Ti-6Al-4 V. They showed a rise of heat tints for shorter ILT as a result of decreasing heat dissipation with increasing build height and decreasing ILT. They declared sufficient ILT for necessary in order to forgo post process heat treatment.

The aforementioned studies were all related to LMD. For L-PBF there are only very few investigations reported. Krauss [28] differentiated three types of thermal cycling in L-PBF influencing the effective cooling rates and, with reference to Kruth et al. [29], the melt pool dimensions: hatch-cycling, which is mainly governed by the length of scan vectors, scan field cycling, which is mainly governed by scanning pattern and strategy, and layer cycling, which is mainly governed by local conditions and exposing parameters. The first and the latter type of thermal cycling are identified as critical. However, an in-depth consideration of layer cycling in terms of the former definition of ILT is missing.

Xu et al. [24] considered ILT as an adjustable parameter for powder bed based AM. They conducted experiments on LPBF of Ti-6Al-4 V. They built cylindric specimens of diameters of between 0.8 mm and 12 mm and a height of 30 mm using four different ILT, i.e., 1 s, 5 s, 8 s and 10 s. Since they did not explicitly define the inter layer time, it is very likely that for recoating a time of about 8 s to 10 s has to be added to the given times to meet the definition of ILT used in this study. Longer ILT had a grain fining effect resulting also in higher yield strength and ultimate tensile strength in their experiments. Lui et al. [25] showed a dependence between the width of alpha-laths and ILT in L-PBF experiments using Ti-6AL-4 V. An increase of ILT results in finer alpha-laths. They mentioned a ILT of 8 s as a limit for this refining effect. Again, the recoating time have to be added to their times, to meet the definition of ILT used in this study.

In light of the published results and the tremendous importance of getting reliable and comparable data about mechanical properties and microstructural development, generation of quantifiable data about the effect of ILT for L-PBF is key to further broaden the fields of application

of AM technologies.

2. Material and methods

2.1. Material and L-PBF processing conditions

The material used in the experiments is a commercial 316 L stainless steel powder with spherical particle morphology. According to supplier information, it has an apparent density of 4.58 g cm^{-3} and a mean diameter of 34.69 µm. The cumulative mass values describe the particle size distribution: D_{10} = 18.22 µm, D_{50} = 30.50 µm, D_{90} = 55.87 µm. The material is processed on a commercial L-PBF system SLM280 HL (SLM Solutions Group AG, Germany), equipped with a single 400 W cw ytterbium fibre laser. The laser melting process runs in argon gas atmosphere with oxygen content below 0.1 %. During the process, a gas flow circulation is established within the machine, where gas flows from the right side of the building chamber to the left. The main gas inlet and the gas outlet are arranged just above the powder bed working plane. In addition, the right face of the building chamber is made of a porous sintered material, which is also part of the gas inlet and establishes a gas flow through the whole building chamber. The gas flow velocity is kept constant during the processes at values of between 19 m/s and 21 m/s, measured in the gas leading pipes by the commercial L-PBF system. All parts are manufactured on a stainless steel substrate plate, which is heated up to 100 °C before and during the process.

2.2. Thermographic measurement set-up

For the thermographic measurements, an infrared camera of the type ImageIR8300 (InfraTec GmbH, Germany) was used. It is sensitive in the spectral range from 2 µm to 5 µm, has a cooled InSb-focal-plane-array as detector and is equipped with a 25 mm objective. The camera has optical access to the build area via a sapphire window in the ceiling of the build chamber. Two mirrors inside the build chamber are used to offset the optical path of the camera to achieve an observation angle close to normal in the front portion of the build area. This physical set-up results in a spatial resolution of approx. 420 µm/pixel in the thermographic images. A subframe image of 160 pixels x 200 pixels was chosen, resulting in an observation field of 68 mm x 85 mm. The framerate of the camera was set to 600 Hz.

The camera is calibrated in different temperature ranges for blackbody radiation. However, due to the window and the mirrors in the optical path as well as the non-ideal emissivity of the observed scenery (powder, build part, molten pool), the temperatures indicated by the camera underestimate the real temperatures. The apparent temperature values of the camera will thus be referred to as IR-signal values in this work. The used integration time was between 45 µs and 193 µs and the bit resolution was set to 14 bit.

2.3. Specimen geometry, scanning strategy and selection of part sections for analysis

As specimen geometry, cuboids of the dimensions (13 × 20 × 114.5) mm^3 were built perpendicular to the build plate, using an alternating meander stripe scanning strategy. The scan vectors proceeded parallel to the edges of the cuboid over the full length of the part without being split into different sections. The scanning pattern was rotated by 90° from layer to layer. All specimens were heat treated after the process and before removal from the plate at 450 °C for 4 h under argon gas atmosphere in order to relieve stresses. After removal from the plate, the specimens were cut into three parts, from which the upper part (the upper 10 mm) and the lower part (the lower 10 mm) were taken for metallographic analysis and hardness measurements. The middle section will be used for further mechanical tests in a subsequent study. Fig. 1 illustrates the specimens' geometry and the scanning strategy and depicts volumes which were taken for metallography. In addition, three layers are highlighted in green colour, for which comparisons of thermographic intensity measurements are analysed in the results chapter. Fig. 1 also sketches the planes of cross sections which were used for metallographic analysis.

While layer thickness, hatch distance and laser power P_L were kept constant over all processes at 50 µm, 120 µm and 275 W, respectively, the scanning velocity v_s was varied (933 mm/s, 700 mm/s, 560 mm/s) resulting in three distinct levels of volumetric energy density (VED, E_v). These are: 49.12 J/mm^3 (low), 65.48 J/mm^3 (standard) and 81.85 J/mm^3 (high). In addition to the scanning velocity, a variation of inter layer times (ILT) was conducted at three distinct levels (short: 18 s; intermediate: 65 s; long: 116 s). It has to be mentioned that the exact times deviate slightly from the given values, as there are differences in the recoating time for odd and even layers and also deviations in the exposing phase due to differences in exposing pattern caused by the 90° rotation of the scanning vectors. However, these variations are below 3 s.

Table 1 summarises the variations of ILT and VED. In the subsequent chapters, the wording "low, standard, high" and "short, intermediate, long" will be used for the description of process conditions as explained above and given in Table 1. The specimens of investigation were built in four different build processes. All specimens of intermediate ILT were built in the same build process. The same is true for long ILT. The short ILT specimens stem from two processes, each containing a complete set of low, standard and high VED specimens. Furthermore, other additional specimens of the same geometry for further investigations were manufactured in the build processes of long and intermediate ILT, which will be analysed elsewhere.

Three specimens fitted into the field of view (FOV) of the infrared camera without being too close to each other, conflicting or shading each other excessively. Therefore, it was possible to observe each level of volumetric energy density for each inter layer time at least once.

Heat accumulation led to increasing temperatures in the upper parts of the specimens. Thus, the blackbody calibration range of the infrared camera was changed during the build process in order to keep the lower limit as low as possible and to avoid overexposure of IR-signals in the regions with high temperature. The comparisons of thermographic data in the result chapter are based on the following blackbody calibration ranges of the IR camera: 200 °C–400 °C, 250° - 500 °C and 300 °C 600 °C. Therefore, IR-signal-time-curves are displayed only within these ranges and data are clipped 10 % above and below the respective thresholds. Thermography data was analysed by using the software IRBIS 3 (InfraTec GmbH, Germany) and Origin 2018 (OriginLab Corporation, USA). For plotting IR-signal-time-curves, average values of three manually chosen pixels that were located in the centre line of the respective part were used for each part. Within each part, IR-signal-time-data were analysed at three distinct layers, which represents different build heights during the process. The analysis was conducted at build heights of 7.5 mm, 30 mm and 113 mm, where the blackbody calibration range of the camera capture was comparable between the different conditions (ILT and VED combinations). Besides, the amount of data could be reduced compared to a continuous analysis over the entire build height.

In addition to the cuboids shown in Fig. 1, one set of three specimens with short ILT at low, standard and high VED was manufactured up to the height of 8.5 mm for further analysis. This set has not been heat treated and has not been observed by the thermography set-up.

2.4. Metallography

For each parameter combination, the upper (Part 4) and lower (Part 1) 10 mm sections (grey parts in Fig. 1) were prepared for metallographic analysis. By cutting the cuboids into three sections, two planes for grinding and polishing have been received as depicted in Fig. 1, from which section I has been polished in separation plane 2 and

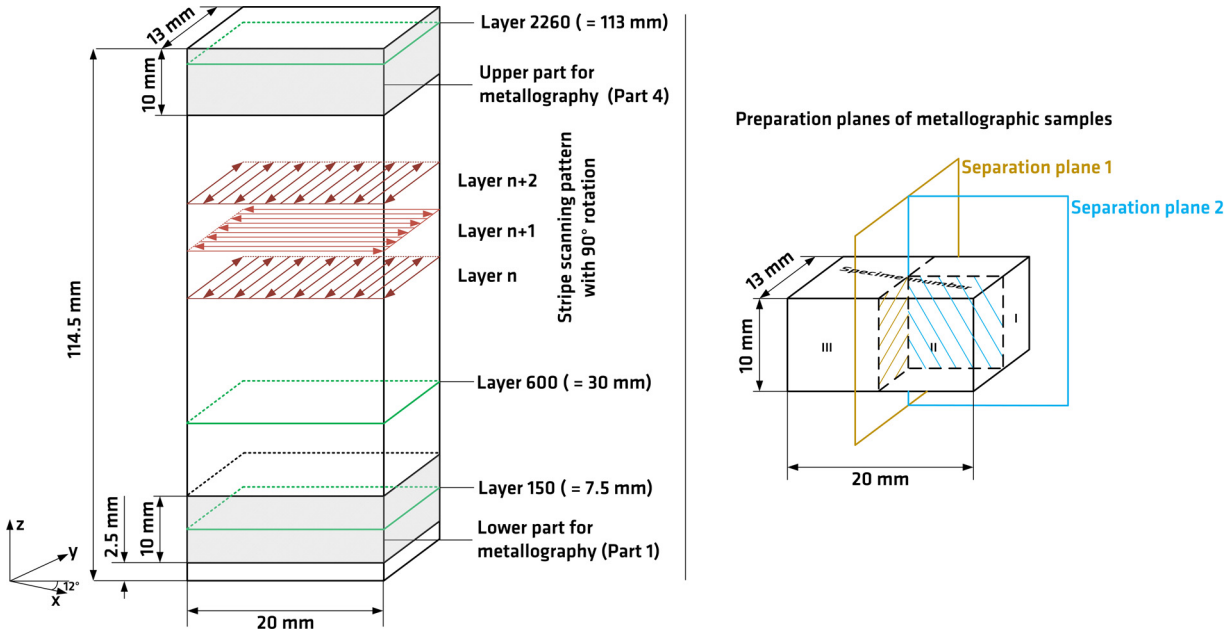

Fig. 1. Left: specimens' geometry and schematic of scanning strategy (red), also highlighting regions of interest (green layers are analysed by thermography, grey volumes are analysed by light-microscopy); Right: planes of metallographic analysis within the grey volumes. (For interpretation of the references to colour in this figure legend, the reader is referred to the web version of this article).

Table 1
Matrix of parameter variation and number of specimens manufactured per parameter combination used in this study.

	Low VED (-25 %) v_s = 933 mm/s P_L = 275 W E_V = 49.12 J/mm^3	Standard VED v_s = 700 mm/s P_L = 275 W E_V = 65.48 J/mm^3	High VED (+25 %) v_s = 560 mm/s P_L = 275 W E_V = 81.85 J/mm^3
Short ILT			
ILT = 18 s	2 specimens built in	2 specimens built in	2 specimens built in 2 build processes
RAE = 1 %	2 build processes	2 build processes	
Intermediate ILT			
ILT = 65 s	2 specimens built in	2 specimens built in	2 specimens built in 1 build process
RAE = 6.1 %	1 build process	1 build process	
Long ILT			
ILT = 116 s	2 specimens built in	2 specimens built in	2 specimens built in 1 build process
RAE = 11.5 %	1 build process	1 build process	

section II has been polished in separation plane 1. Unetched cross sections were taken for optical light microscopy in order to determine porosity by grey value analysis using the software IMS Client V17Q1 (Imagic Bildverarbeitung AG, Glattbrugg, Switzerland). A threshold value of 136 was chosen for all cross sections. Subsequently, cross sections were colour etched using Beraha II etching detergent for 10–30 s. A determination of the sub-grain structure was conducted by line intercepts of low angle grain boundaries. For each set of parameters, the determination was conducted at both separation planes of both parts for at least three different micrographs. Seven horizontal lines and seven vertical lines were used for this method in accordance to DIN EN ISO 643 [30]. Melt pool depths were determined at Part 4 plane II by measuring ten melt pools of the last exposed layer. Vickers hardness testing HV1 was conducted at both planes of both parts with 25 indentations per plane arranged in a 5 × 5 matrix using a hardness tester EmcoTest DuraScan 70G5 (EMCO-TEST Prüfmaschinen GmbH, Austria).

3. Experimental results

3.1. Macroscopy

From a macroscopic point of view, no significant differences can be noticed between specimens of build processes of long and intermediate ILT. In contrast, tempering colours occurred on the surfaces of specimens of build processes of short ILT. Differences in the outer appearance were not only noticeable between the distinct build processes but also between the three different parts of each of the two short ILT build processes, which were exposed by different energy parameters. When exposed by the high volumetric energy density, specimens showed a blue colour on their surfaces. Specimens exposed by the standard volumetric energy density showed red to brown colour and specimens exposed by the low energy density appeared yellowish. Fig. 2 shows photographs of each top surface in a matrix arrangement corresponding to Table 1. The strongest effect emerged at the top surface of the specimens but can also be noticed over a wide range of the side surfaces with some fluctuations within the height, as can be seen on the right in Fig. 2. The onset of the predominant tempering colour of each part did not start before the first 10 mm–15 mm of the specimens.

3.2. Thermography

From a thermographic point of view, significant differences in IR-signal-time-curves can be seen between the distinct combinations of ILT and VED. In addition, the build height also influences the gradient of these cooling curves significantly. Both can be read from the plots in

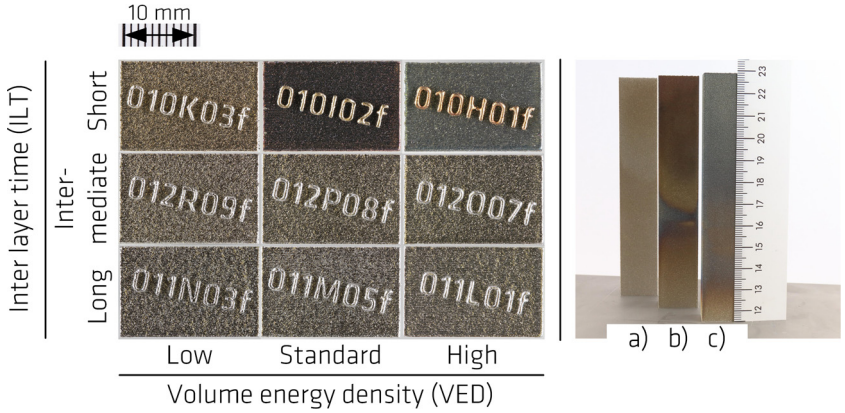

Fig. 2. Left: Comparison of top surface tempering colours of the complete parameter matrix (compare to Table 1). Right: backside of the specimens of a build process with short ILT and a) low, b) standard, c) high VED.

Fig. 3. As mentioned above, the apparent temperature values of the camera cannot be regarded as real temperatures, since the camera calibration does not consider the different optical elements in the set-up and, most importantly, is only valid for blackbody radiators. Therefore, the apparent temperature values are regarded as IR-signal values. Despite that fact, they allow for relative comparison of the cooling behaviour.

The shown curves are calculated as mean values of three pixels in the centre line of the corresponding specimens. To trace the cooling behaviour of single spatial points of the specimens' surface, the shown curves are calculated as mean values of three pixels in the centre line of the corresponding specimens. This ensures that there is no IR-signal levelling over the entire surface, due to the very rapid cooling down of the melt tracks and the high number of scanning vectors. If in contrast, a mean value of the total surface or a mean value of an area smaller than the total surface but much larger than the melt tracks had been taken, this would have levelled the maximum corresponding IR-signal values, due to contributions of already cooled areas or areas which are still not exposed. To avoid contributions of mad pixels, the standard deviations were calculated for the respective pixels. As the focus of the

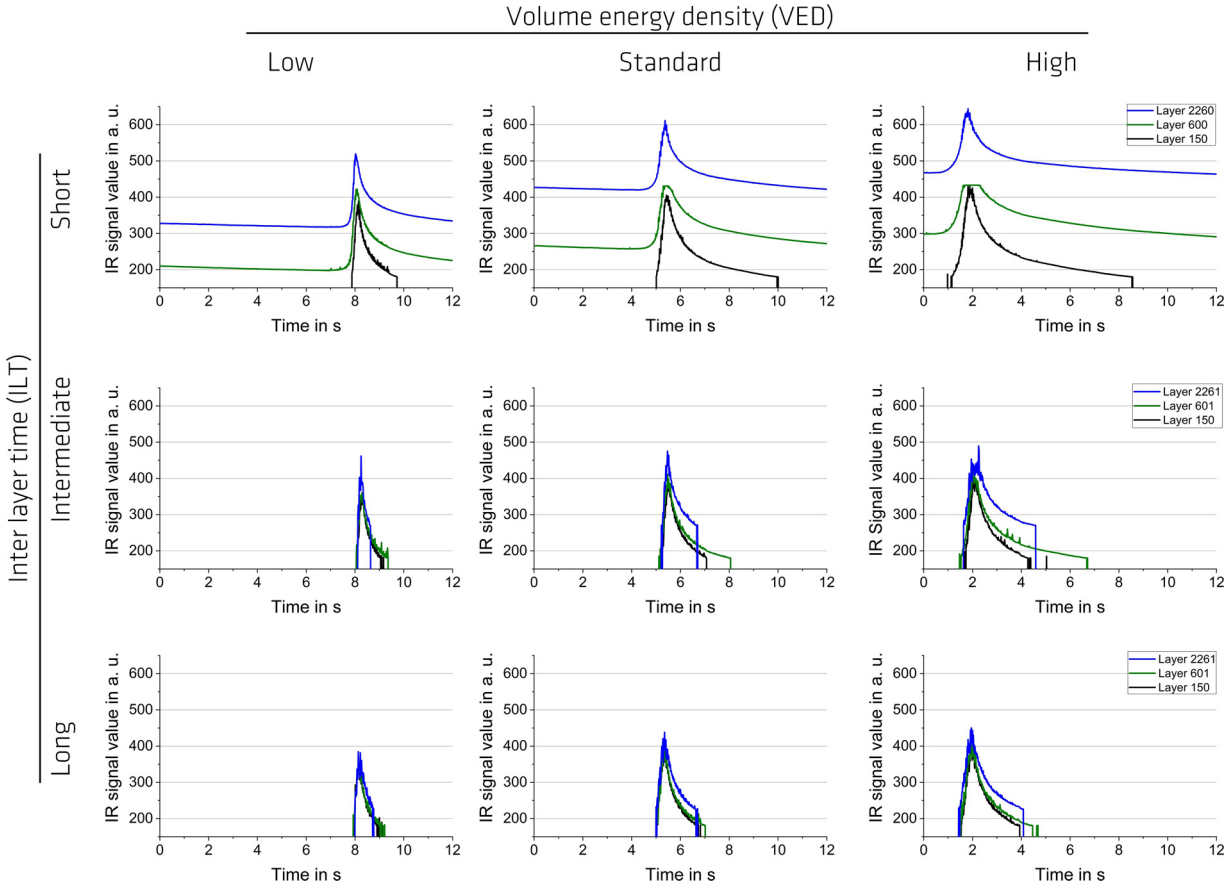

Fig. 3. IR-signal-time-plots of complete parameter matrix. Three lines indicate three different build heights of the measuring position: z = 7.5 mm (black), z = 30 mm (green), z = 113 mm (blue). The data are clipped 10 % above and below the blackbody calibration range. The time stamp starts at the beginning of the capturing (t = 0), which can deviate between the processes. (For interpretation of the references to colour in this figure legend, the reader is referred to the web version of this article).

analysis is set on the cooling curves, only contributions after the peak signals were used for this calculation. The mean standard deviation between the signal values of the chosen pixels ranges between 1.6 and 14.4 which is small compared to the IR-signal values of between 200 and 600. Possible edge effects are not in the focus of this study, as it focuses on the bulk properties of the specimens produced. All quantitative examinations of this study (microstructure, melt-pool depth, porosity, hardness) were made at the inner of the specimens. Therefore, a comparison of IR-signals based on pixels of the centre line is a valid and easy solution.

The IR-signal-time-curves of the specimens of the same ILT are extracted from the same thermographic sequence, in which the three parts are exposed one after the other within the FOV of the camera, starting with the high VED. Hence, the melting peaks appear at different times for different VED. The peak IR-signals of the melt pools are out of the blackbody calibration range for all investigated combinations Besides, the utilised camera does not have the spatial resolution and frame rate to resolve the melt pool IR-signals correctly. Therefore, the melt pool IR-signals are not considered here.

In Fig. 3, the following can be observed: Firstly, for almost all parameter combinations, a decrease in cooling rate with increasing build height can be found. Only for the combination of long ILT and low VED, no significant change can be noticed. Secondly, cooling rates decrease with increasing energy density. Thirdly, cooling rates decrease with decreasing ILT, which can be seen more clearly in Fig. 4, where the IR-signal-time-curves for the standard VED at different heights and different ILT are depicted. It is worth noting that, apart from short ILT, all curves start below the lower limit of the blackbody calibration range. However, IR-signal-time-plots at higher build heights (here: 60 mm and 113 mm) and short ILT show a slowly decreasing IR-signal plateau at limits well above the IR-signals of the platform preheating temperature before the melting peaks arise. In addition, this pre-melting IR-signal plateau increases with increasing build height and increasing VED. Thus, the part does not cool down to a temperature (represented by an IR-signal) below the lower calibration range of the camera between exposure of subsequent layers in these cases. A more quantitative analysis is given in Section 4.2.

3.3. Microscopy

3.3.1. Microstructure

Light-microscopic analysis of the microstructure reveals differences in the average apparent sub-grain size for distinct parameter combinations. Fig. 5 depicts the measured average apparent sub-grain areas for every parameter combination at two different heights of the specimens as explained in Fig. 1.

According to Krakhmalev et al. [31], Birnbaum et al. [32] and Saeidi [33], the microstructure of L-PBF manufactured 316 L material consists of two characteristic types of boundaries at the micrometre range of size: Classical high-angle grain boundaries, called colony

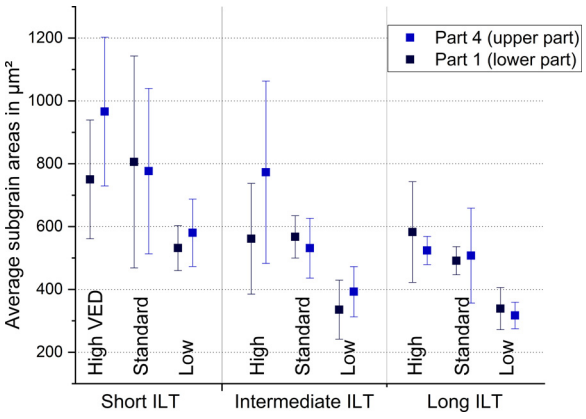

Fig. 5. Average sub-grain size depending on parameter combinations and build height.

boundaries by Krakhmalev et al. [31]. Adjacent colonies have different crystallographic orientations and appear in different colours in electron back scattered diffraction (EBSD) measurements. The second type of boundary are boundaries between cells, which form one colony. The cells have only slight differences in crystallographic orientation and their boundaries are, therefore, regarded as low-angle grain boundaries [31].These low-angle grain-boundaries were identified as thick dislocation structures [34]. Additionally, local solute segregation to these cell walls was recently claimed by Birnbaum et al. [32], who presented atomic force microscopy (AFM) measurements showing that cell walls protruding from the surface in etched condition, which is not possible for pure dislocation structures without solute segregation.

A differentiation between the low-angle and high-angle grain boundaries is difficult by the means of optical light-microscopy. Therefore, both types of boundaries were marked at the intercepts with the horizontal or vertical lines according to the norm DIN EN ISO 643 [30] in the conducted measurements. The measured feature is regarded as apparent sub-grain size in this study.

The measured average apparent sub-grain areas are between 237 µm² and 1482 µm². Additionally, Fig. 6 shows micrographs taken from Part 4 of short ILT at each of the three VED levels and a micrograph of the intermediate ILT at standard VED as reference. Despite partly overlapping values of standard deviations, two clear trends can be seen in Fig. 5: Firstly, sub-grain sizes decrease with decreasing VED in the upper areas of the specimen, i.e., Part 4 sections. Secondly, sub-grain sizes increase with decreasing ILT. However, the differences between intermediate ILT and long ILT are small for particular VEDs and have to be considered very carefully in light of a relatively high measurement uncertainty. While no significant differences in sub-grain sizes between upper and lower parts can be shown for standard and low VED, sub-grain sizes of parts exposed by high VED tend to increase over build height for short and intermediate ILT. A more detailed characterisation

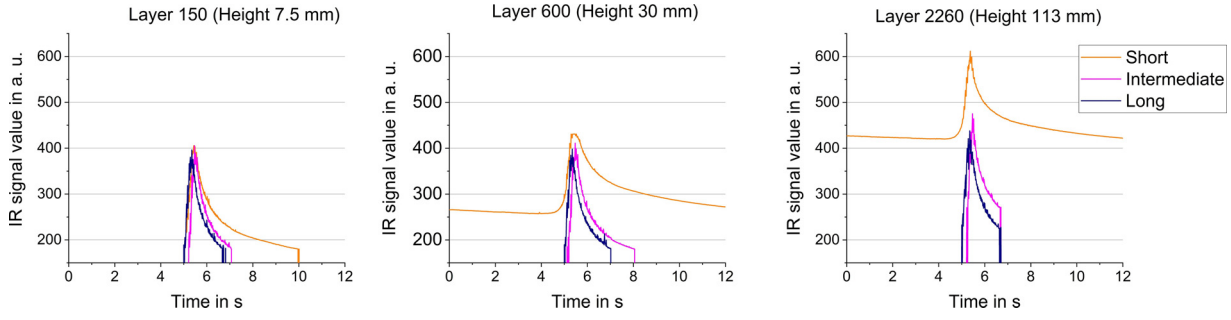

Fig. 4. IR-signal-time-plots at Standard VED for different build heights. Three lines indicate three different ILT: short (yellow), intermediate (magenta), long (blue). The data are clipped 10 % above and below the calibration range. The time stamp starts at the beginning of the capturing (t = 0), which can deviate between the processes. (For interpretation of the references to colour in this figure legend, the reader is referred to the web version of this article).

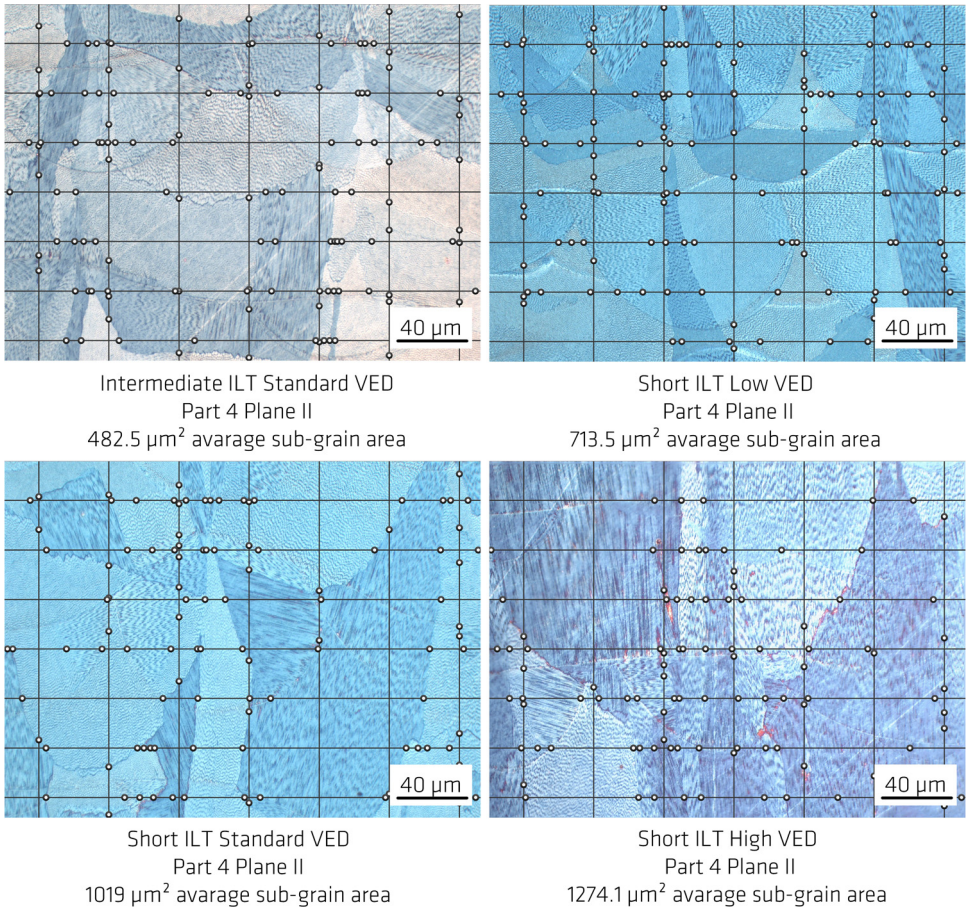

Fig. 6. Micrographs taken from Part 4 sections of short ILT at each of the three VED levels and one micrograph of Part 4 section of intermediate ILT at standard VED as reference. Horizontal and vertical lines were used for sub-grain size determination, white dots show line intercepts with low-angle grain boundaries.

of the microstructure by EBSD and scanning electron microscopy (SEM) measurements will be conducted in a subsequent study.

Comparing the mean values of average sub-grain areas for the same ILT, the increase from low to high VED parts can be quantified by 66 % (short ILT), 97 % (intermediate ILT) and 65 % (long ILT) for the upper parts. A calculated comparison of mean values of average sub-grain areas for the same VED between short and intermediate ILT reveals an increase of 25 % (high VED), 40 % (standard VED) and 48 % (low VED).

3.3.2. Melt pool depths

Significant differences in the penetration depth of the laser are found for the investigated VED levels, resulting in different melt pool geometries and melt pool depths. Fig. 7 shows the melt pool depths of the last layer of the specimens for every parameter combination. It also displays the corresponding micrograph of the standard combination of parameters (intermediate ILT, standard VED). Melt pool depths between 145 µm and 424 µm have been measured. A similar trend is observable for each ILT: the depth of the melt pool increases by approx. 26 % for high VED compared to the standard VED and it decreases by approx. 34 % for low VED compared to standard VED.

Not only from the depth of the melt pools but from their shape and aspect ratios of depth to width, a change of welding modes from transition to deep penetration welding can be observed between the different energy inputs. Low VED results in transition mode, whereas standard and high VED result in deep penetration mode with an aspect ratio of up to approx. 2. This change can be noticed for every ILT.

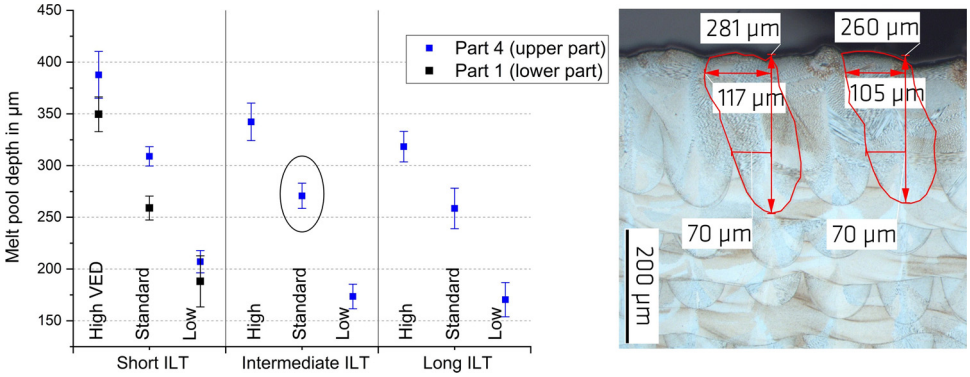

Fig. 7. Melt pool depths depending on parameter combinations and build height. Cross section belongs to the encircled data point for standard VED and intermediate ILT.

Furthermore, an increase in melt pool depth with decreasing ILT can be noticed at the values of the upper parts (Part 4). When comparing melt pool depths for long and intermediate ILT, no significant increase is measurable as it is smaller than the standard deviation. However, a clear increase of 13 % to 19 % can be measured between corresponding energy densities of short and intermediate ILT. Fig. 7 also shows melt pool depths of the lower part for short ILT, which were determined from measurements of the separate non-heat-treated specimens. These specimens were only built up to 8.5 mm in height. A clear drop of the depth compared to the upper part can be noticed. The melt pool depths of the lower part for short ILT are well within the range of the melt pool depths measured at the upper parts for intermediate and long ILT.

3.3.3. Porosity

Porosity values for the lower parts of the specimens are at a very low level of 0.1 % to 0.2 % for all parameter combinations. Without claiming any significance, it is interesting to notice that porosity values of 0.2 % are observable only for one of the two cross sections of Part 1 at high VED and short ILT and high VED and intermediate ILT. All other cross sections show only 0.1 % porosity. In contrast, porosity values of the upper parts of the specimens show increased porosities for all parts manufactured with high VED. However, the degree of increase changes with changing ILT. For long ILT, only a slight increase of porosity up to 0.3 % can be noticed, similar to intermediate ILT. The specimen manufactured with short ILT and high VED shows porosity values of 1.1 % and 2.7 %. Fig. 8 illustrates the described trends by unetched cross sections. The morphology of inspected pores is mainly spherical and is regarded to keyhole porosity as can be seen in the magnification of the etched cross section at the right in Fig. 8. A change of the porosity determination threshold (see Section 2.4) by 10 % led up to a difference of 0.3 in the porosity determination for higher total porosity values (greater than 1 %) but did not change values of low total porosity. Therefore, the presented relative comparison by grey value analysis of optical light microscopy images seems to be useful without the claim of absolute numbers, which could be collected by Archimedes' principle.

3.4. Hardness

Hardness measurements reveal differences between upper and lower part of the specimens as shown in Fig. 9. There is a slight trend towards lower hardness values at the upper parts for all parameter combinations. However, the hardness differences between lower and upper part are small for long ILT, but they increase with decreasing ILT. This decrease gets very significant for short ILT, showing a hardness drop of 6 % to 20 % depending on VED. In contrast, no significant change in hardness values of the lower part can be noticed when comparing corresponding VEDs at different ILT. Only a slight increase in hardness can be noticed for low VED compared to high and standard VED in the lower parts for all ILT and in the upper parts for intermediate and long ILT. Contrasting with this is a significant drop of hardness with increasing VED for short ILT. The most significant difference in hardness within one specimen can be noticed for high VED and short ILT showing a hardness of 221 HV1 in the lower part and 176 HV1 in the upper part. It is worth noting that many of the hardness indentations showed distorted edges, as is exemplarily shown in Fig. 9. However, the requirement of less than 5 % difference between the two diagonals were met pursuant to DIN EN ISO 6507-1 [35] for all measuring points.

4. Discussion

All experimental results show a similar trend of an interplay between decreasing ILT and increasing VED towards lower thermal gradients and accumulation of heat, leading to extreme values regarding melt pool behaviour, microstructure, porosity and mechanical properties. Additionally, this trend is intensified by an increase in build height, which will be discussed in the following sections.

4.1. Relevance of ILT and RAE for real part applications

Taking the standard values of scanning velocity (v_s = 700 mm/s) and hatch distance (h_S = 0.12 mm) as well as a continuous stripe scanning strategy as reference, the chosen ILT represents the following ratios of area exploitation (RAE): 1.1 %, 6.1 %, 11.6 %. Using the example of a demonstrator pressure vessel as an AM component, the relevance of the chosen ILT for real parts can be proven. They are well within a realistic range of RAE of real component build volumes. Fig. 10 shows the demonstrator part arranged on a base plate (left) cut into seven parts, which are shown as cross-sections on the right. For each of the seven resulting cross-sections, Table 2 depicts the respective ILT and RAE for two cases: case 1 represents the build-up of only one pressure vessel within the machine, case 2 represents the simultaneous build-up of four pressure vessels within one build process. For the calculation of ILT values, the single laser machine SLM280 HL was used as reference. The table compares the ILT and the RAE of the experimental part of this study (case 3) with the theoretical values for the two cases of the pressure vessel production.

4.2. Quantification of thermographic measurements

The resulting properties of the specimens, manufactured under different ILT and VED conditions, will be discussed in the light of the analysed in-situ thermography data of the build processes. Costa et al. [12] explained in the context of a LMD process simulation that during the ILT, "the deposited material cools down, essentially due to heat conduction to the substrate", which is connected with the effect of

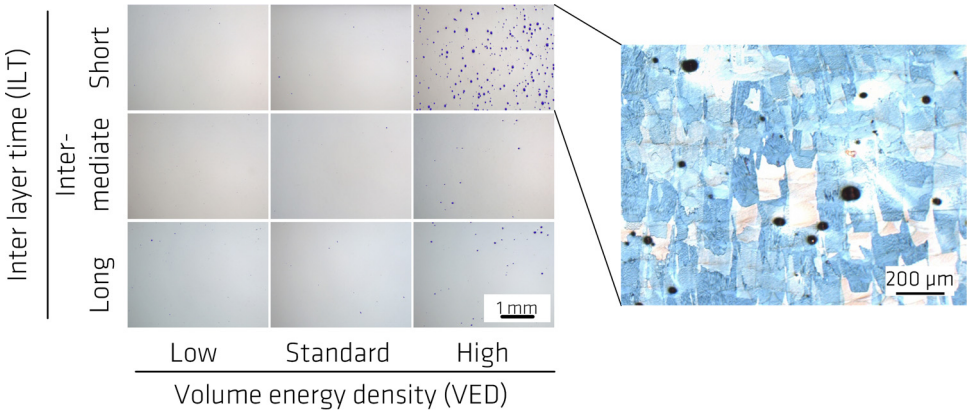

Fig. 8. Cross sections showing porosity in the respective upper parts (Part 4) depending on parameter combinations.

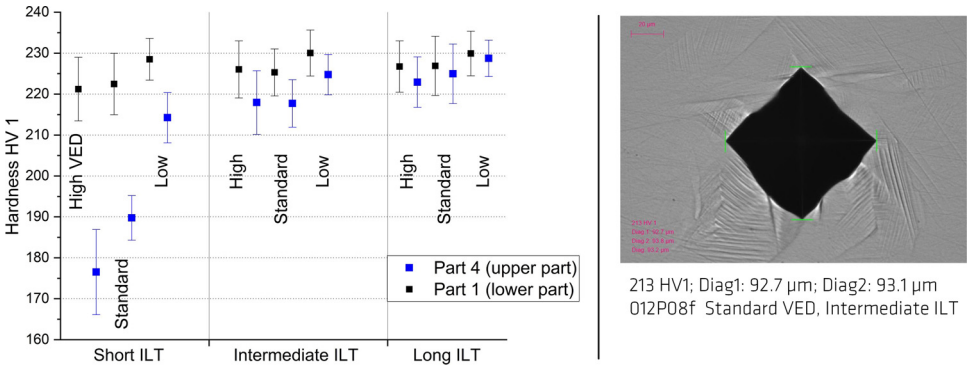

Fig. 9. Left: hardness values depending on parameter combinations and build height. Right: light microscopy of a hardness indentation showing distorted edges.

increasing average temperatures during the build-up for decreasing ILT, resulting in progressively growing melt pool sizes. This can be directly observed by the analysis of the IR-signal curves (Fig. 3). All curves exhibit IR-signal peaks at the time when the laser passes the pixels chosen for analysis with subsequent cooling down. The cooling curves allow for a direct comparison between the different parameter combinations and, in addition, between the different build heights. Regardless of the VED, a clear trend for longer cooling down times for decreasing ILT can be observed. Fig. 4 displays IR-signal curves for standard VED at different ILT for each of the analysed heights. On the one hand, the qualitative comparison of the cooling curves works well between high VED, upper regions of the part, short ILT and the other conditions. On the other hand, the differences between intermediate ILT and long ILT are not displayed very clearly in the figures in every case. For this reason, a quantitative analysis enables a better comparison. Therefore, cooling times between IR-signal values of 380 and 280 have been calculated, called T4/3. This is according to typical cooling time evaluation in welding technology between 800 °C and 500 °C (T8/5). The IR-signal values of 380 and 280 were chosen since both values are within the IR-signal ranges of the blackbody camera calibrations for most of the measurements and are also passed during the measurement time of one layer in many of the cases. The respective T4/3 times are displayed in Table 3 for standard and high VED. The numbers are discussed in the following sections.

Unpublished work using the same thermography camera in a very similar set-up on the same L-PBF machine indicates that the IR-signal values, when taken as apparent temperature in °C, strongly underestimate the real temperatures. However, the informative value of a relative comparison of cooling times using these values remains valid. In-process calibration efforts are planned and will be published elsewhere soon.

Table 2
Typical ILT and RAE of a demonstrator part in comparison to the experiments of this study.

	Case 1: One part per build process		Case 2: Four parts per build process		Case 3: Experiments of this study		
Cross-section	ILT in s	RAE in %	ILT in s	RAE in %		ILT in s	RAE in %
1	9.5	0.2	13.9	0.6	Short	18	1.1
2	46.2	4.1	160.9	16.4	Intermediate	65	6.1
3	61.3	5.7	221.0	22.8	Long	116	11.6
4	34.4	2.8	113.5	11.3			
5	15.9	0.9	39.7	3.4			
6	10.9	0.3	19.4	1.2			
7	9.3	0.1	13.0	0.5			

4.3. Discussion of long and intermediate ILT

The values in Table 3 show that the differences in T4/3 times between long and intermediate ILT are quite small, i.e., below 0.2 s in the lower and middle part of the specimens. In the upper part of the specimens the differences and the absolute values are considerably larger. A heating up of the growing part over the build-up height, which is expected to lead to increasing T4/3 times, is evident even for long ILT in this quantitative analysis. Nonetheless, no obvious differences can be found in the outer appearance of specimens manufactured at long and intermediate ILT. There are also no significant differences between these two ILT at the same VED levels with respect to microstructure

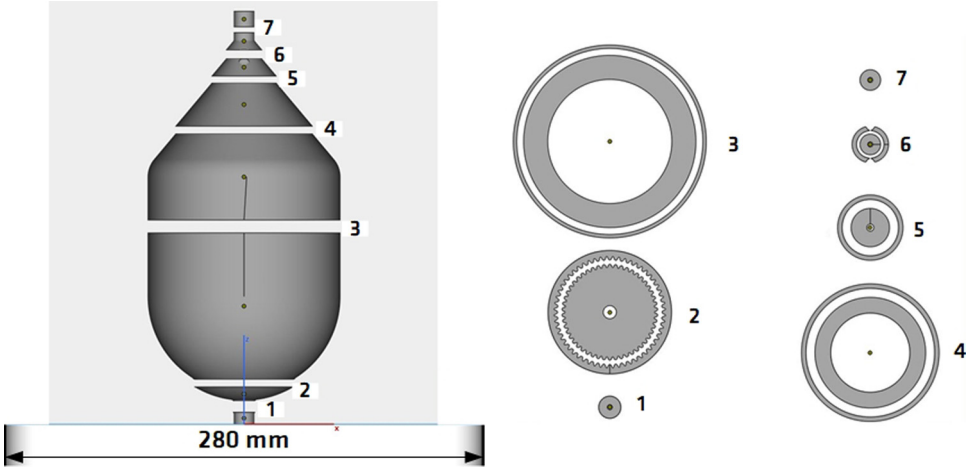

Fig. 10. Side view and cross sections of a 3D-CAD model of a demonstrator pressure vessel real part component.

Table 3
T4/3 times for cooling down from 380 to 280 (IR-signal values) in s for different parameter combinations and build heights.

ILT	Build height 7.5 mm		Build height 30 mm		Build height 113 mm	
	VED					
	Standard	High	Standard	High	Standard	High
Short	0.59	0.8	4.77	10.19*	**	**
Intermediate	0.3	0.48	0.4	0.6	0.9	1.52
Long	0.25	0.37	0.25	0.42	0.52	0.65

* Cooling down time to an IR-signal of 282 before recoater moves.
** No cooling to below an IR-signal of 380.
Time calculation error approx. 0.05 s.

(Section 3.3.1) visible by optical light microscopy. The reason for that is assumed to be in the cooling times, which are still comparably fast (T4/3 below 2 s).

However, for high VED, a slight increase in sub-grain sizes over the part height can be noticed at intermediate ILT (Section 3.3.1). This corresponds to the longest T4/3 cooling time within the long and intermediate ILT parameter combinations, which can be found for high VED and intermediate ILT in the upper region. The respective T4/3 time is three-times higher than in the lower part. Although the parts cool down below the blackbody calibration limit of the camera within a short time, which is considerably less than the given ILT, the longer T4/3 time and resulting slower cooling rates appear to influence the solidification process in terms of an onset of initial sub-grain growth due to less undercooling. Zitelli et al. [36] resume from Keshavarzkermani et al. [37] a grain size decrease for higher cooling rates forced by lower laser power. Constitutional supercooling leads to cellular mode of crystallisation at high solidification rates and steep thermal gradients [31]. A change of the letter by heat accumulation is able to change the feature sizes such as cell spacing [31].

Regarding the results of measurements of the melt pool depths (Section 3.3.2), the same general trend can be noticed when comparing long and intermediate ILT: in the upper part, the values are at a similar level for each corresponding VED, only a slight increase for high VED at intermediate ILT can be recognised. The same pattern exists for hardness measurements (Section 3.4), apart from a slight hardness drop at high VED and intermediate ILT and at standard VED in the upper parts. The described differences are small, as they have all partly overlapping error bars. This is illustrated in each corresponding figure in Section 3. Hence, it can be summarised that in cases of long and intermediate ILT the inter layer time does not influence the properties of the part when a standard VED parameter set, or lower VED, is applied. This is also reflected by the very low porosity values at these parameter combinations.

A graphical summary of the influences of the ILT, VED and build height for long and intermediate ILT is given in Table 4. The following first conclusion can be drawn: under “normal” conditions, at least ILT greater than 65 s or RAE greater than 6.1 % do not influence the quality of the part over its entire build height. An in-depth investigation of ILT thresholds requires further experiments or simulation-based presumptions. However, when applying higher VED, the mentioned ILT is short enough to allow for a slight change in properties over the build height, due to accumulation of heat. This essentially acts as an elevation of the build platform preheating temperature. More realistic part shapes with geometrical bottlenecks for heat conduction to the base plate are expected to increase this effect. In addition, in this case, the occurrence of porosity is possible, which would not occur in smaller specimens, such as cubes of 10 mm edge length, that are widely produced for parameter optimisation and material qualification.

4.4. Discussion of short ILT in comparison to intermediate and long ILT

In contrast to the rather small differences between long and intermediate ILT parameter combinations, the IR-signal-time-plots of the short ILT combinations (Figs. 3 and 4) reveal major and significant differences in terms of longer cooling times and higher IR-signal values. Hence, the T4/3 times are significantly longer than for long and intermediate ILT. The T4/3 times for all VED combinations at short ILT in the upper part cannot be calculated, since the IR-signals do not drop below the respective IR-signals before the next layer is recoated.

Although the calculated T4/3 values at build height of 7.5 mm (lower part, Part 1) for short ILT are higher than for intermediate ILT, they are still in the same range of magnitude. Consistently, the melt pool depths of the lower part for short ILT are similar to the melt pool depth at the upper part for intermediate and long ILT between the corresponding VED pairs. The same qualitative pattern can be recognised for hardness values of the lower part. Furthermore, no significant porosity increase can be noticed in the lower part for the short ILT combinations, compared to the two longer ILT. However, a clear increase in sub-grain size occurs when comparing short ILT and the two longer ILT. A similar range of sub-grain size which is developed by

Table 4
Graphical summary of influences on the measures at long and intermediate ILT.

	Decreasing ILT (from long to intermediate) without build height effect, i.e., close to base plate	Increasing VED at long and intermediate ILT without build height effect, i.e., close to base plate	Increasing build height at long and intermediate ILT and constant VED
T4/3 time	↗	↗	↗
Tempering colours	→	→	→
Sub-grain size	→	↑	→
Melt pool depth	→	↑	Not measured
Porosity	→	→	→
Hardness	→	→	→

↑ significant increase.
↗ slight increase.
→ constant.
↓ significant decrease.

Table 5
Graphical summary of influences on the measures at short ILT.

	Decreasing ILT (from intermediate to short ILT) without build height effect, i.e., close to base plate	Increasing VED at short ILT without build height effect, i.e., close to base plate	Increasing build height at short ILT
T4/3 time	↑	↑	↑
Tempering colours	→	→	↑
Sub-grain size	↑	↑	*
Melt pool depth	Not measured	↑	↑
Porosity	→	→	↑
Hardness	→	→	↓

↑ significant increase.
↗ slight increase.
→ constant.
↓ significant decrease.
*Effect is difficult to show in this table, as build height contributes to longer holding times of in-situ heat treatment, which might be able to affect the whole part in this measure.

standard VED and intermediate or long ILT occurs at low VED using short ILT. The same is true for standard VED at short ILT and high VED at longer ILT. This again is assumed to be induced by less undercooling during solidification.

These characteristics change drastically over the build height of the specimens for short ILT: a clear hardness drop is exhibited in the upper part of the specimens for each VED parameter. Furthermore, an increase in melt pool depth can be noticed. Both effects can be directly related to a progressive heating of the build part during the process, since the short ILT does not allow for sufficient cooling down of the part before the next layer is exposed. The effect of heat accumulation becomes apparent from the T4/3 values and the respective IR-signal-time-plots. In layer 600 (i.e. build height 30 mm), there is already no cooling down below the lower limit of the chosen blackbody calibration range of the camera between subsequent exposing phases. This, in turn, acts as in-situ heat treatment of the part.

The tempering colours, observed at the short ILT specimens (Fig. 2), are in line with this explanation since they usually occur at specific holding temperatures. In the absence of comparisons of tempering colours for different temperatures at the same oxygen content at which the L-PBF machine runs, a direct deduction of colour deduced temperatures as calibration mean for the IR-signals of the thermographic measurements is not possible. However, the occurrence and difference in tempering colours within the same build processes are in line with the difference in the measured in-situ or in-process holding temperatures of the part, represented by IR-signal values. This can be understood in terms of the known interplay between the supply of oxygen and the supply of heat for the development of tempering colours. The supply of oxygen is expected to be at the same level for the distinct specimens which are produced in the same build process, due to the controlled argon flooding of the build chamber.

No significant sub-grain size differences over the build height of the specimen can be seen by the microstructure analysis (Section 3.3.1). The sub-grain size in the lower part appears similar to that of the upper part, although a cooling down of the part between subsequent layers to values below the lower calibration limit of the camera was still observable in the lower part. Therefore, a kind of continuous sub-grain growth in the entire specimen might have also contributed in addition to the initial differences in undercooling of the melt, due to an in-process heat treatment induced by the distinct heat accumulation in upper layers. Krakhmalev et al. [31] reported the disappearance of cell boundaries after heat treatment at 900 °C of 15 min, beginning at 850 °C. They directly correlated this disappearance with an experimentally observed hardness drop. They also claimed cell boundary stability at 800 °C [31]. For better understanding of the in-situ heat treatment observed in this study it is worth noting that the time between layer 600 and layer 2260 for short ILT was around 8.3 h. Therefore, the time for diffusional processes is much longer than in the above cited short term heat treatments of 15 min. However, the manual measurement of apparent sub-grain sizes is connected to a high degree of uncertainty, which is illustrated in the scale of the error bars in Fig. 5. Further measurements using EBSD and SEM will be useful to support the assumption of continuous sub-grain growth in the entire part. Besides, some residual stress measurements will also give answer to the question, if stress relaxation due to this in-situ heat treatment might have contributed to the hardness drop. Lastly, already planned IR camera calibration attempts will help to estimate the real temperatures of the specimens.

Another important outcome of the investigation of the short ILT is the strong increase of the occurrence of defects in the form of porosity over the build height. Porosity values of about 1.1 % and 2.7 % are found at the upper part of high VED specimens. The occurrence of this porosity is most likely caused by the increase in melt pool depth and temperature caused by the lack of sufficient cooling down in-between consecutive exposures and can be regarded as keyhole porosity. This porosity might lead to a weakening of the mechanical properties of the part. It might also play an additional role in the hardness drop of the upper parts.

A graphical summary of the influences of the ILT, VED and build height for intermediate and short ILT is given in Table 5.

4.5. Heat accumulation over build height as in-situ heat treatment

The build height was identified to be an important factor in the L-PBF processing of 316 L when there is an interplay with ILT. However, when considering the build height separately without any interplay with other factors, its effect can be easily overlooked or underestimated. This can be comprehended, when only looking at long ILT or intermediate ILT, where no or only slight effects over the build height are observed in this study. Therefore, it is not surprising to find published results pointing out similar grain sizes for 316 L [38] and similar melt pool geometries for IN718 [39] over the entire build height. This is undoubtedly true for the objects of investigation, as either the chosen geometry does not consist of enough layers to show any effect or the chosen ILT is long enough for sufficient cooling down between subsequent layers. Information on the latter factor is often missing.

However, for short ILT, the heat accumulation over build height plays an important role in terms of defect formation, melt pool geometry and hardness as discussed in Section 4.4. The last column of Tables 4 and 5 summarises these effects. In many cases, when only small cubes of, e.g., 10 mm edge length are built for parameter studies, the effects will not appear, as heat accumulation over subsequent layers is comparably small in the lower regions of a part. This underestimation might then prove harmful in the case of large real part applications. Specific temperature regions, which are prone to onset precipitations, depletions by element segregation or phase separation, must therefore

be considered individually for the chosen material. In the case of 316 L, attention should be given to the possible embrittlement at 475 °C, when small fractions of delta ferrite may develop in the predominately austenitic microstructure. To investigate this issue in more detail, phase identification by EBSD is planned for the produced specimens of this study.

4.6. Potential actions to enhance comparability of L-PBF components and their properties

Short ILT in combination with a relevant build height has been identified as a critical factor for heat accumulation during the L-PBF process. The resulting changes in local temperatures are able to affect microstructure, melt pool behaviour, hardness and defect density. Small RAE can be often found in complex shaped real part applications, which stresses the importance of the issue. Manufacturing the same part in different batch sizes per build process is also often practiced and directly affects the ILT. Therefore, questions arise regarding comparability of part quality of those parts as well as representativeness of specimens for real part properties, as they might experience completely different thermal histories.

An easy and safe solution would be the application of cooling pauses between subsequent layers for those layers with small RAE. For this to become practically viable, a minimum time would first have to be identified. This would make manufacturing slow and expensive and would also contradict approaches for higher build rates, e. g. through a parallelisation of the recoating and exposition step. An adaptive set of parameters would be a smarter solution. However, this needs further progress in pre-simulation and the capability of deeper machine control. An alternative solution could be the implementation of a suitable thermography set-up, implementing an adaptive time between layers by cooling below a threshold value prior to the next exposure. In terms of comparability between specimens and real part applications, the development of new specimen geometries, which represent critical features of the real part geometry, seems to be a desirable goal. In addition, a transfer of the thermal history of a real part or its most critical sections on a standard specimen by means of adapted parameter combinations, used to manufacture this specimen, could be another possible solution towards safe AM applications. In any case, thermography appears to be an adequate instrument to identify critical areas in-situ as well as for proving the transferability of thermal histories to other geometries.

5. Conclusions

In this study, the importance of ILT and build height for part quality and properties of L-PBF components has been highlighted. Additionally, scanning parameters resulting in different VED were considered. Geometry in its easiest modification, i.e., build height, and ILT can induce significant differences in part quality and its properties. Using the example of a pressure vessel, the relevance of the chosen inter layer times has been illustrated.

The following major variations have been shown:

- a significant heat accumulation over the build height for short ILT resulting in an increase of cooling times greater than factor 12,
- differences in sub-grain size of up to a factor 6 depending on chosen parameter combinations for fully dense parts,
- an increase of 40 % in sub-grain size between short and intermediate ILT for standard VED,
- an increase of the melt pool depth over the build height for short ILT of up to 20 %,
- the occurrence and increase of keyhole porosity in growing parts for short ILT,
- a hardness drop of up to 20 % over the build height for short ILT.

In contrast to the small differences for longer ILT, it must be concluded that small RAE, as they occur in complex shaped real part applications, are a source of inhomogeneities and defects as they are able to change the local temperatures due to less time for part cooling. This must be considered in real part production. Due to the identified differences in microstructure, questions arise regarding the comparability of part quality, when manufacturing the same part in different batch sizes per build process. Furthermore, questions arise in relation to the representativeness of specimens for real part properties, as they might experience completely different thermal histories. This applies even when they are manufactured with the same set of parameters and in the same build process. Not only microstructural features, which might get homogenised by appropriate post process heat treatment are affected, but also part density. This amplifies the importance of the issue even more. Improvements on this issue can be found in the identification of a minimum ILT, which ensures comparability at the expense of productivity. Adapted parameter combinations would be the smarter solution to overcome the problem. They might also help transferring critical thermal histories during the manufacture of real part applications to the manufacture of specimen geometries. The calibration of the IR camera set-up will help to get reliable temperature information and will improve the discussion of the findings. Besides EBSD and SEM analysis will enable the identification of changes in microstructure in more detail.

CRediT authorship contribution statement

Gunther Mohr: Conceptualization, Methodology, Validation, Formal analysis, Investigation, Data curation, Writing - original draft, Writing - review & editing, Visualization. **Simon J. Altenburg:** Methodology, Resources, Writing - review & editing. **Kai Hilgenberg:** Conceptualization, Writing - review & editing, Supervision.

Declaration of Competing Interest

None.

Acknowledgements

The authors would like to thank Mareike Kirstein and Anna Lena Seibel for their very helpful support in the metallography laboratory of BAM division 9.3 and BASF SE, Germany, for the generous provision of 3D-CAD data of a part demonstrator of a pressure vessel.

This research was funded by BAM within the focus area Materials.

References

[1] T. DebRoy, H.L. Wei, J.S. Zuback, T. Mukherjee, J.W. Elmer, J.O. Milewski, A.M. Beese, A. Wilson-Heid, A. De, W. Zhang, Additive manufacturing of metallic components – process, structure and properties, Prog. Mater. Sci. 92 (2018) 112–224.

[2] D. Herzog, V. Seyda, E. Wycisk, C. Emmelmann, Additive manufacturing of metals, Acta Mater. 117 (2016) 371–392.

[3] T.T. Wohlers, Wohlers Report. 3d Printing and Additive Manufacturing State of the Industry, Wohlers Associates, Fort Collins, 2017.

[4] D. Bourell, J.P. Kruth, M. Leu, G. Levy, D. Rosen, A.M. Beese, A. Clare, Materials for additive manufacturing, CIRP Ann. Manuf. Technol. 66 (2) (2017) 659–681.

[5] A.B. Spierings, K. Dawson, M. Voegtlin, F. Palm, P.J. Uggowitzer, Microstructure and mechanical properties of as-processed scandium-modified aluminium using selective laser melting, CIRP Ann. Manuf. Technol. 65 (1) (2016) 213–216.

[6] M. Karg, B. Ahuja, S. Kuryntsev, A. Gorunov, M. Schmidt, Processability of high strength aluminium-copper alloys AW-2022 and 2024 by laser beam melting in powder bed, Proceedings of the 25th Annual International Solid Freeform Symposium, Austin, USA, 2014.

[7] G. Mohr, J. Johannsen, D. Knoop, E. Gärtner, K. Hummert, C. Emmelmann, Processing of a high-strength Al-Fe-Ni alloy using laser beam melting and its potential for in-situ graded mechanical properties, Lasers in Manufacturing Conference, Munich, Germany, 2017.

[8] U. Zerbst, K. Hilgenberg, Damage development and damage tolerance of structure maanufactuired by selective laser melting - a review, Procedia Struct. Integr. 7 (2017) 141–148.

[9] G. Schulze, Die Metallurgie des Schweißens, Springer, Berlin Heidelberg, 2010.
[10] K. Kempen, B. Vrancken, L. Thijs, S. Buls, J. Van Humbeeck, J.-P. Kruth, Lowering thermal gradients in Selective Laser melting by pre-heating the baseplate, Solid Freeform Fabrication Symposium Proceedings, Austin, USA, 2013.
[11] M. Shiomi, K. Osakadaa, K. Nakamuraa, T. Yamashitaa, F. Abeb, Residual stress within metallic model made by selective laser melting process, CIRP Ann. 53 (1) (2004) 195–198.
[12] L. Costa, R. Vilar, T. Reti, A.M. Deus, Rapid tooling by laser powder deposition: process simulation using finite element analysis, Acta Mater. 53 (14) (2005) 3987–3999.
[13] A. Yadollahi, N. Shamsaei, S.M. Thompson, D.W. Seely, Effects of process time interval and heat treatment on the mechanical and microstructural properties of direct laser deposited 316L stainless steel, Mater. Sci. Eng. A 644 (2015) 171–183.
[14] R. Jendrzejewski, G. Śliwiński, Investigation of temperature and stress fields in laser cladded coatings, Appl. Surf. Sci. 254 (4) (2007) 921–925.
[15] E.R. Denlinger, J.C. Heigel, P. Michaleris, T.A. Palmer, Effect of inter-layer dwell time on distortion and residual stress in additive manufacturing of titanium and nickel alloys, J. Mater. Process. Technol. 215 (2015) 123–131.
[16] M. Pavan, M. Faes, D. Strobbe, B. Van Hooreweder, T. Craeghs, D. Moens, W. Dewulf, On the influence of inter-layer time and energy density on selected critical-to-quality properties of PA12 parts produced via laser sintering, Polym. Test. 61 (2017) 386–395.
[17] M. Möhrle, Gestaltung von Fabrikstrukturen für die additive Fertigung, Springer, 2018.
[18] P. Hartogh, T. Vietor, Vorhersage der Fertigungszeit und-kosten für die additive Serienfertigung, Additive Serienfertigung, Springer, 2018, pp. 69–87.
[19] N. Kretzschmar, I.F. Ituarte, J. Partanen, A decision support system for the validation of metal powder bed-based additive manufacturing applications, Int. J. Adv. Manuf. Technol. 96 (9) (2018) 3679–3690.
[20] V. Griffiths, J.P. Scanlan, M.H. Eres, A. Martinez-Sykora, P. Chinchapatnam, Cost-driven build orientation and bin packing of parts in Selective Laser Melting (SLM), Eur. J. Oper. Res. 273 (1) (2019) 334–352.
[21] A. Chergui, K. Hadj-Hamou, F.J.C. Vignat, I. Engineering, Production scheduling and nesting in additive manufacturing, Comput. Ind. Eng. 126 (2018) 292–301.
[22] P. Karimi, E. Sadeghi, D. Deng, H. Gruber, J. Andersson, P. Nylen, Influence of build layout and orientation on microstructural characteristics of electron beam melted Alloy 718, Int. J. Adv. Manuf. Technol. 99 (9-12) (2018) 2903–2913.
[23] L. Papadakis, D. Chantzis, K. Salonitis, On the energy efficiency of pre-heating methods in SLM/SLS processes, Int. J. Adv. Manuf. Technol. 95 (1-4) (2018) 1325–1338.
[24] W. Xu, E. Lui, A. Pateras, M. Qian, M.J.A.M. Brandt, In situ tailoring microstructure in additively manufactured Ti-6Al-4V for superior mechanical performance, Acta Mater. 125 (2017) 390–400.
[25] E.W. Lui, W. Xu, A. Pateras, M. Qian, M. Brandt, New development in selective laser melting of Ti–6Al–4V: a wider processing window for the achievement of fully lamellar α + β microstructures, JOM 69 (12) (2017) 2679–2683.
[26] B. Torries, S. Shao, N. Shamsaei, S. Thompson, Effect of Inter-layer Time Interval on the Mechanical Behavior of Direct Laser Deposited Ti-6Al-4V, (2016), pp. 1272–1282.
[27] F. Spranger, B. Graf, M. Schuch, K. Hilgenberg, M. Rethmeier, Build-up strategies for additive manufacturing of three dimensional Ti-6Al-4V-parts produced by laser metal deposition, J. Laser Appl. 30 (2) (2018) 022001.
[28] H. Krauss, Qualitätssicherung beim Laserstrahlschmelzen durch schichtweise thermografische In-Process-Überwachung, Herbert Utz Verlag, 2017.
[29] J.P. Kruth, G. Levy, F. Klocke, T.H.C. Childs, Consolidation phenomena in laser and powder-bed based layered manufacturing, CIRP Ann. 56 (2) (2007) 730–759.
[30] DIN, DIN EN ISO 643: Stahl - Mikrophotographische Bestimmung der erkennbaren Korngröße, (2013).
[31] P. Krakhmalev, G. Fredriksson, K. Svensson, I. Yadroitsev, I. Yadroitsava, M. Thuvander, R. Peng, Microstructure, solidification texture, and thermal stability of 316 L stainless steel manufactured by laser powder bed fusion, Metals 8 (8) (2018).
[32] A.J. Birnbaum, J.C. Steuben, E.J. Barrick, A.P. Iliopoulos, J.G. Michopoulos, Intrinsic strain aging, Σ3 boundaries, and origins of cellular substructure in additively manufactured 316L, Addit. Manuf. 29 (2019) 100784.
[33] K. Saeidi, Stainless Steels Fabricated by Laser Melting, Scaled-down Structural Hierarchies and Microstructural Heterogeneities, PhD Department of Materials and Environmental Chemistry, Stockholm University, Stockholm, Sweden, 2016.
[34] P. Krakhmalev, I. Yadroitsava, G. Fredriksson, I. Yadroitsev, In situ heat treatment in selective laser melted martensitic AISI 420 stainless steels, Mater. Des. 87 (2015) 380–385.
[35] DIN, DIN EN ISO 6507-1: Metallische Werkstoffe-Härteprüfung nach Vickers-Teil 1: Prüfverfahren, Beuth, Berlin, 2006.
[36] Folgarait Zitelli, S. Di, Laser powder bed fusion of stainless steel grades: a review, Metals 9 (7) (2019).
[37] A. Keshavarzkermani, E. Marzbanrad, R. Esmaeilizadeh, Y. Mahmoodkhani, U. Ali, P.D. Enrique, N.Y. Zhou, A. Bonakdar, E. Toyserkani, An investigation into the effect of process parameters on melt pool geometry, cell spacing, and grain refinement during laser powder bed fusion, Opt. Laser Technol. 116 (2019) 83–91.
[38] A. Leicht, U. Klement, E.J.M.C. Hryha, Effect of build geometry on the microstructural development of 316L parts produced by additive manufacturing, Mater. Charact. 143 (2018) 137–143.
[39] B. Cheng, J. Lydon, K. Cooper, V. Cole, P. Northrop, K. Chou, Melt pool sensing and size analysis in laser powder-bed metal additive manufacturing, J. Manuf. Process. 32 (2018) 744–753.